

A JWST investigation into the bar fraction at redshifts $1 \leq z \leq 3$

Zoe A. Le Conte,¹★ Dimitri A. Gadotti,¹ Leonardo Ferreira,² Christopher J. Conselice,³
Camila de Sá-Freitas,⁴ Taehyun Kim,⁵ Justus Neumann,⁶ Francesca Fragkoudi,⁷ E. Athanassoula,⁸
and Nathan J. Adams³

¹Centre for Extragalactic Astronomy, Department of Physics, Durham University, South Road, Durham DH1 3LE, UK

²Department of Physics & Astronomy, University of Victoria, Finnerty Road, Victoria, British Columbia, V8P 1A1, Canada

³Jodrell Bank Centre for Astrophysics, University of Manchester, Oxford Road, Manchester M13 9PL, UK

⁴European Southern Observatory, Karl-Schwarzschild-Str. 2, D-85748 Garching bei Muenchen, Germany

⁵Department of Astronomy and Atmospheric Sciences, Kyungpook National University, Daegu, 41566, Republic of Korea

⁶Max-Planck-Institut für Astronomie, Königstuhl 17, D-69117 Heidelberg, Germany

⁷Institute for Computational Cosmology, Department of Physics, Durham University, South Road, Durham DH1 3LE, UK

⁸Aix Marseille Univ, CNRS, CNES, LAM, Marseille, France

Accepted XXX. Received YYY; in original form ZZZ

ABSTRACT

The presence of a stellar bar in a disc galaxy indicates that the galaxy hosts a dynamically settled disc and that bar-driven processes are taking place in shaping the evolution of the galaxy. Studying the cosmic evolution of the bar fraction in disc galaxies is therefore essential to understand galaxy evolution in general. Previous studies have found, using the Hubble Space Telescope (HST), that the bar fraction significantly declines from the local Universe to redshifts near one. Using the first four pointings from the James Webb Space Telescope (JWST) Cosmic Evolution Early Release Science Survey (CEERS) and the initial public observations for the Public Release Imaging for Extragalactic Research (PRIMER), we extend the studies on the bar fraction in disc galaxies to redshifts $1 \leq z \leq 3$, i.e., for the first time beyond redshift two. We only use galaxies that are also present in the Cosmic Assembly Near-IR Deep Extragalactic Legacy Survey (CANDELS) on the Extended Groth Strip (EGS) and Ultra Deep Survey (UDS) HST observations. An optimised sample of 768 close-to-face-on galaxies is visually classified to find the fraction of bars in disc galaxies in two redshift bins: $1 \leq z \leq 2$ and $2 < z \leq 3$. The bar fraction decreases from $\sim 18.9^{+9.7}_{-9.4}$ per cent to $\sim 6.6^{+7.1}_{-5.9}$ per cent (from the lower to the higher redshift bin), but is $\sim 3 - 4$ times greater than the bar fraction found in previous studies using bluer HST filters. Our results show that bar-driven evolution commences at early cosmic times and that dynamically settled discs are already present at a lookback time of ~ 11 Gyrs.

Key words: galaxies: bar – galaxies: evolution – galaxies: disc – galaxies: general – galaxies: high-redshift – galaxies: distances and redshifts

1 INTRODUCTION

Stellar bars are one of the most abundant features in local disc galaxies (e.g., Eskridge et al. 2000; Marinova & Jogee 2007; Aguerri et al. 2009; Buta et al. 2015), providing insight into the internal evolutionary processes taking place in these galaxies. Several investigations using optical surveys in the immediate Universe find strong stellar bars in about a third of disc galaxies (e.g., Barazza et al. 2009; Nair & Abraham 2010; Masters et al. 2011). This fraction increases to 60 – 80 per cent with the inclusion of weaker bars (e.g., de Vaucouleurs et al. 1991; Menéndez-Delmestre et al. 2007; Sheth et al. 2008; Erwin 2018).

Barred stellar structures in disc galaxies are thought to form relatively quickly, over times of the order of a hundred million years, in massive disc galaxies which are dynamically cold and rotationally supported (e.g., Hohl 1971; Kalnajs 1972; Ostriker & Peebles

1973; Sellwood & Wilkinson 1993). Hence, the formation of stellar bars is an indicator of the evolutionary stage of a galaxy. The bar is a dense central region of evolved stellar populations on highly eccentric orbits (e.g., Weinberg 1985; Contopoulos & Grosbol 1989; Athanassoula 1992; Kormendy & Kennicutt 2004). The non-axisymmetric nature of stellar bars is due to the very elongated form of the orbits that constitute the bar, which would be the x_1 orbital family or one of the higher multiplicity families, both parallel to the semi-major axis of the bar (Contopoulos & Papayannopoulos 1980; Wang et al. 2022), which have such properties. The orbital composition of the bar, coupled with the fact that the bar can be viewed from all possible angles, introduces a range of observed ellipticities. Therefore, the shape of the stellar bar in disc galaxies can appear shorter and more oval or longer and rectangular, thus influencing the bar strength measurement. The torque of the stellar bar redistributes the angular momentum within the galaxy (e.g., Lynden-Bell & Kalnajs 1972; Athanassoula 2003; Athanassoula 2005). This makes bars a primary and efficient driver of internal evolution through the redistribution

★ E-mail: zoe.a.le-conte@durham.ac.uk

of baryonic and dark matter (e.g., [Menéndez-Delmestre et al. 2007](#); [Regan et al. 2006](#); [Di Matteo et al. 2013](#); [Fragkoudi et al. 2018](#)). Bar-driven gas inflow considerably impacts central galactic star formation, most notably in the formation of stellar structures, such as the nuclear disc (e.g., [Sanders & Tubbs 1980](#); [Knapen et al. 1995](#); [Allard et al. 2006](#); [Coelho & Gadotti 2011](#); [de Lorenzo-Cáceres et al. 2012](#); [Bittner et al. 2020](#); [Gadotti et al. 2020](#)). The bar also undergoes buckling processes forming box/peanuts (e.g., [Combes & Sanders 1981](#); [Combes et al. 1990](#); [Ishizuki et al. 1990](#); [Kormendy 1982](#); [Kormendy & Kennicutt 2004](#); [Carles et al. 2016](#)). It is currently disputed as to whether the presence of a bar could influence the fueling mechanisms of the active galactic nucleus (AGN) although a consensus is emerging in that bars help building a fuel reservoir near the galactic centre (e.g., [Knapen et al. 1995](#); [Alonso et al. 2013](#); [Cisternas et al. 2015](#); [Alonso et al. 2018](#); [Silva-Lima et al. 2022](#); [Garland et al. 2023](#)). [Sheth et al. \(2005\)](#) confirm the result of [Sakamoto et al. \(1999\)](#), namely that the central kiloparsec of barred galaxies contains a higher degree of molecular gas concentrations, however in simulations [Fragkoudi et al. \(2016\)](#) observe a consequential reduction in the gas inflow to the central kiloparsec due to the boxy/peanut bulge associated with the bar.

Multiple observational investigations into the abundance of stellar bars in disc galaxies up to $z \approx 1$ find a linear decrease in their frequency with increasing redshift. A constant bar fraction out to $z \sim 1$ in the Galaxy Evolution from Morphologies and SEDs (GEMS) survey was found in [Jogee et al. \(2004\)](#) where three independent techniques were used to identify spiral galaxies and ellipse fits were used to characterise barred galaxies. [Abraham et al. \(1999\)](#) found a decline in the bar fraction from quantitatively estimated bar strengths of galaxies in the Hubble Deep Field-North and -South. [Sheth et al. \(2003\)](#) identified barred galaxies by ellipse fitting techniques for galaxies $z > 0.7$ in the Near-Infrared Camera and Multi-Object Spectrometer (NICMOS) Hubble Deep Field-North. Using the 2 deg² Cosmic Evolution Survey (COSMOS), [Sheth et al. \(2008\)](#) found a decrease in the bar fraction using cross-checked visual and ellipse fitting bar identification techniques. A decrease by a factor of two at $z \sim 1$ in the COSMOS bar fraction was found in [Melvin et al. \(2014\)](#) using visual classifications. It has then been inferred from these studies that bar features cease to exist at greater lookback times, implying that bar-driven evolutionary processes do not commence until ~ 6 Gyr after the Big Bang. These studies require high-resolution and sensitive imaging across a large sky area, which the Hubble Space Telescope (HST) has achieved. At $z \approx 1.5$, [Simmons et al. \(2014\)](#) discover prominent bars in massive disc galaxies and suggests that at $\sim z > 1$, the bar fraction is sustained at ~ 10 per cent. Two observational studies of the evolution of the bar fraction with redshift find no sign of a sharp decline at $z > 0.7$: [Elmegreen et al. \(2004\)](#) find a near constant bar fraction of 0.23 ± 0.03 at redshifts up to $z = 1.1$ on a sample of 186 disc galaxies; [Jogee et al. \(2004\)](#) find the optical bar fraction of $\sim 0.3 \pm 0.06$ to remain at redshifts up to $z \sim 1$.

In cosmological simulations, [Kraljic et al. \(2012\)](#) found a depletion in the number of bars in present-day spiral progenitors beyond $z \approx 1$, implying a violent phase of galaxy evolution where discs are dynamically hot, and there are excessive merger events. However, [Athanassoula et al. \(2016\)](#) follow the merging of two disc galaxies and found the merger remnant starts forming a bar before the disc is fully developed. [Rosas-Guevara et al. \(2022\)](#) use TNG50 simulations ([Nelson et al. 2019](#)) to trace the bar fraction evolution with redshift and show the bar fraction to increase to ~ 50 per cent at $z \approx 1$ and only significantly decrease at $\sim z > 2$. Even at $z \approx 6$, the simulated bar fraction, at a minimum, reaches ~ 25 per cent. The bar fraction found in the Auriga cosmological zoom-in simulations from

[Fragkoudi et al. \(2020\)](#) are in good agreement with observational studies, where for redshifts $0 \leq z \leq 1.5$ the bar fraction decreases from ~ 70 per cent to ~ 20 per cent.

Various bar identification techniques can be applied to images, including classifications by eye (e.g., [Athanassoula et al. 1990](#); [Cheung et al. 2013](#); [Simmons et al. 2014](#); [Buta et al. 2015](#)). Stellar bar characterisation and analysis identified structural features by eye from the colour composite images of galaxies, where participants vote a galaxy as *barred*, *candidate bar* or *unbarred* (e.g., [de Vaucouleurs et al. 1991](#); [Eskridge et al. 2000](#); [Nair & Abraham 2010](#); [Buta et al. 2015](#)). Characteristic signatures in the radial profiles of barred galaxies can be seen, which can be used to aid or replace visual classification methods. Position angle (PA) and ellipticity (e) measurements are obtained from isophotal ellipse fits (see § 3.1 for an explanation), in which the parameter radial profiles are used to identify a bar feature. The criteria for bar identification differs between studies but generally agrees that within the bar-dominated region, the PA remains constant, and e gradually rises. Studies can choose to determine the end of the bar as one of three metrics or by taking the average of these positions: the peak ellipticity, the minimum ellipticity succeeding the peak ellipticity, and a significant change in the PA (e.g., [Wozniak et al. 1995](#); [Buta et al. 1998](#); [Elmegreen et al. 2004](#); [Jogee et al. 2004](#); [Marinova & Jogee 2007](#); [Guo et al. 2023](#)). In a volume-limited $z \leq 0.01$ SDSS/DR7 sample with galaxies $M_r \leq -15.2$, [Lee et al. \(2019\)](#) found visual classification methods to detect a higher number of weaker bars than ellipse fitting techniques and Fourier analysis. Additionally, in their study, they concluded that ellipse fitting techniques could miss $\sim 15\%$ of visually classified bars due to large bulges in early-type spirals. Using a deep convolutional neural network, [Abraham et al. \(2018\)](#) identified bars in SDSS with good accuracy. Surveys are now on remarkably large scales, so automated techniques such as machine learning (e.g., [Cheng et al. 2021](#)) will become vital for morphological classifications.

The James Webb Space Telescope (JWST) has provided the opportunity to expand the investigation of the bar fraction to higher redshifts. Imaging from the Near Infrared Camera (NIRCam) probes the rest-frame near-infrared (NIR) emission of galaxies at redshifts up to 3 and probes the rest-frame optical at redshifts up to 7; NIR emission traces the older stellar populations which dominate bar features and are also less affected by dust extinction and new star formation. (e.g., [Frogel et al. 1996](#); [Schneider 2006](#)). In fact, the NIR bar fraction at $z \approx 0$ is higher than the optical bar fraction (e.g., [Marinova & Jogee 2007](#)), and [Buta et al. \(2015\)](#) argues that this is due to stellar structural features being more perceptible. Thus, weaker bars in the optical become stronger in the NIR, so a higher bar fraction is observed. In addition, the primary mirror on JWST is over 2.5 times the diameter size of the HST primary mirror, meaning that the sensitivity of JWST is significantly improved. The improved sensitivity, along with the longer rest-frame wavelengths probed by JWST, means elongated bar structures become more discernible than in their counterpart HST images (e.g., [Huertas-Company et al. 2023](#)). For this reason, we can now propel our understanding of bar-driven evolution with JWST by searching for the epoch when stellar barred structures form in disc galaxies.

A previous study of stellar bars at $\sim z > 1$ using the Cosmic Evolution Early Release Science Survey (CEERS) was conducted by [Guo et al. \(2023\)](#) who quantitatively identified six strongly barred galaxies at $z \sim 1 - 3$, with the highest redshift galaxy at $z \sim 2.3$. In this study, we use the initial four NIRCam JWST observations from CEERS to find the evolution of the bar fraction at redshifts between $z = 1 - 3$. To this aim, we visually classify a mass-complete sample

of these high-resolution rest-frame NIR images for barred features in disc galaxies.

This paper is outlined as follows: in § 2, we explain the NIRCам image reduction pipeline and our sample selection. Stellar bar identification techniques and our methodology for visual classifications are discussed in § 3. In § 4, we present the bar fraction for two redshift bins, $z = 1 - 2$ and $z = 2 - 3$, and § 5 discuss the implications of our findings on when bar-driven evolution commences and, finally, § 6 summarises this study. Throughout this study, we assume the latest Planck flat Λ CDM cosmology with $H_0 = 67.36$, $\Omega_m = 0.3153$, and $\Omega_\Lambda = 0.6847$ (Planck Collaboration et al. 2020).

2 THE PARENT SAMPLE

To define our sample, we use the initial four public NIRCам JWST observations from the Cosmic Evolution Early Release Science Survey (CEERS; PI: Finkelstein, ID=1345, Finkelstein et al. 2023, CEERS1, CEERS2, CEERS3 and CEERS6) taken in June 2022 that overlap with the Cosmic Assembly Near-IR Deep Extragalactic Legacy Survey (CANDELS; Grogin et al. 2011; Koekemoer et al. 2011) on the Extended Groth Strip field (EGS), as well as the initial public observations for the Public Release Imaging for Extragalactic Research (PRIMER; PI: Dunlop, ID=1837, Dunlop et al. 2021), that overlap with the CANDELS Ultra Deep Survey (UDS) Field observations.

Together, the data covers $\sim 30 \text{ arcmin}^2$ of an area with CANDELS HST overlap. The raw data was reduced independently using a custom set-up of the JWST pipeline as described in § 2.1. Our sample selection based on HST CANDELS catalogues is provided in § 2.2.

2.1 Data Reduction Pipeline

We reprocess all of the uncalibrated lower-level JWST data products following a modified version of the JWST official pipeline. This is similar to the process used in Adams et al. (2023) and exactly the same reductions as used in Ferreira et al. (2022), which can be summarised as follows: (1) We use version 1.6.2 of the pipeline with the Calibration Reference Data System (CRDS) version 0942 which was the most up-to-date version at the time these data products were generated. Use of CRDS 0942 is essential for zero point issues as discussed in Adams et al. (2023). (2) We apply the $1/f$ noise correction derived by Chris Willott on the resulting level 2 data of the JWST pipeline.¹ (3) We extract the sky subtraction step from stage 3 of the pipeline and run it independently on each NIRCам frame, allowing for quicker assessment of the background subtraction performance and fine-tuning. (4) We align calibrated imaging for each individual exposure to GAIA using `tweakreg`, part of the `DrizzlePac` python package.² (5) We pixel-match the final mosaics with the use of `astropy reproject`. The final resolution of the drizzled images is $0.03 \text{ arcseconds/pixel}$.

Furthermore, an additional step was added for the PRIMER reductions in step (2) above due to the presence of a significant stripping pattern artefact at a 45-degree angle in the NIRCам footprint, resembling the diffraction pattern of a bright star outside the field of view of the camera. This issue was removed with an adaptation of the $1/f$ noise algorithm, first rotating the observations to 45 degrees to align the pattern with one of the axes, followed by a background

subtraction for each row based on the background mean of that row. Finally, the adjusted file is rotated back to its original orientation. This drastically reduces the artefact in the final products, although some are still visible in colour composites due to the non-uniform nature of the artefact across different NIRCам filters. Galaxy stamps that present these residual artefacts are flagged during subsequent classification as described in § 3.3.

Each one of the four June CEERS observations was processed into individual mosaics, while the PRIMER UDS observations were stacked in a single mosaic due to the large overlapping area.

A description of the sample selection is given in § 2.2.

2.2 Sample Selection

As a way to produce a selection with robust photometric redshifts and stellar masses, we use the CANDELS-based catalogues produced by Duncan et al. (2019) that include observations from HST, Spitzer, and other ground-based facilities. These redshifts are robustly calibrated from spectroscopic redshifts, with an average outlier fraction of $\frac{|\Delta z|}{1+z_{spec}} \sim 5\%$ (see Duncan et al. 2019 for details).

From these catalogues, we select all sources that lie within the footprint of the CEERS and PRIMER observations outlined previously. All sources with photometric redshifts and stellar masses that are present in both CANDELS and the new JWST observations are selected. Additionally, no magnitude or signal-to-noise cut is done to mitigate any selection bias due to different sensitivities between HST and JWST, which prevents JWST bright galaxies from being excluded if they are faint in HST bands. Then, all overlapping sources between $1 \leq z \leq 6$ are selected, resulting in a total sample of 7111 galaxies present within the combined area of CEERS+PRIMER, including 3956 galaxies with visual Hubble type classifications from Ferreira et al. (2022) at $z > 1.5$.

For each of the 7111 galaxies in the sample, we produce 30 mas 128×128 pixel cutouts from the HST ACS CANDELS filters available, namely F606W and F814W, as well as for the JWST filters, namely F115W, F150W, F200W, F277W, F356W and F444W. For the HST Wide Field Camera 3 filters, namely F125W and F160W, we produce 60 mas 64×64 pixel cutouts covering a consistent angular field of view, enabling us to probe the same galaxies in a similar wavelength regime between the two instruments. However, note that the resolution varies between the JWST F150W filter and the HST WFC3 F160W filter, for example. In this study, we select the F444W JWST filter and compare these galaxies to their HST WFC3 filter F160W. To observe the evolution of the bar fraction, the sample is cut to sources between the redshifts $1 \leq z \leq 3$, resulting in a parent sample of 5218 galaxies in the JWST F444W filter and 5445 galaxies in the HST F160W filter. We note that some galaxies fall in the gaps between the NIRCам detectors, and therefore, while they are included in the HST sample, they cannot be analysed with JWST data.

3 BAR IDENTIFICATION

The random orientation of galaxies challenges observational attempts of bar measurements. Stellar bars are distinguishable in near-face-on galaxies and become less defined in high-inclination galaxies.

This study aims to determine the fraction of disc galaxies that harbour a bar in an optimised sample of F444W NIRCам and F160W WFC3 images. In § 3.1, the optimisation of the parent sample is explained, while the search for disc galaxies and the derivation of the fraction of disc galaxies in the sample is given in § 3.2. Finally, in

¹ <https://github.com/chriswillott/jwst>

² <https://github.com/spacetelescope/drizzlepac>

§ 3.3, the bar classification method used on the optimised sample is discussed. For our bar identification process, we use visual inspection of galaxy images as well as of PA and e radial profiles.

3.1 Sample Optimisation

Considering the challenges involved in the identification of bars, as noted above, we choose to remove highly inclined and overly faint or poorly resolved galaxies from the sample through an automated process. To do so, we fit ellipses to the isophotal contours of all galaxies in the parent sample to extract radial profiles of e and PA (see, e.g., Gadotti et al. 2007; Barazza et al. 2008, 2009; Aguerri et al. 2009). Figure 1 shows in the left panel the ellipse fits superposed on the F444W NIRCcam image of the galaxy EGS_23205, and in the right panel, radial profiles of the e and PA of the fitted ellipses. EGS_23205 is an example of a barred galaxy in this study and is observed relatively face-on.

Before visually classifying galaxies as barred or unbarred, we apply a three-step procedure to obtain our final, optimised galaxy sample containing galaxies in which a bar can be identified robustly: (1) ellipse-fitting to NIRCcam images without fixing the centre; (2) second ellipse-fitting with fixed centres; (3) removal of highly inclined galaxies. In the following, we give a detailed explanation of these three steps:

Phase 1 Elliptical isophotes are fitted to F444W NIRCcam images of the JWST galaxy sample and analysed using `photutils.isophote` from Python’s `astropy` package (Bradley et al. 2022). This package uses an iterative method to measure the isophotes (Jedrzejewski 1987). Approximately 30% of the parent sample had successful ellipse fits in the F444W filter. The remaining $\sim 70\%$ of galaxies that failed ellipse fittings are poorly resolved and/or low surface brightness systems and are removed from the sample.

Phase 2 The ellipses fitted in the previous step do not have a specified centre, which may prevent the correct identification of highly inclined galaxies. We thus take the inner 10 to 40 per cent of the isophotes fitted to the galaxy in the first step and take the average position of the centre of these isophotes as the galaxy centre. The choice for this range of radii ensures that one has enough pixels to compute a statistically robust position of the galaxy centre and simultaneously avoids strongly asymmetric structures, which are often at larger radii. We then re-run `photutils.isophote` on F444W NIRCcam galaxy images with fixed specified central positions. With fixed centres, the ellipse fits failed for approximately 8% of the parent sample. We verified that the failed ellipse fits correspond to galaxies with overly irregular morphology or images of point sources conspicuously showing the JWST point spread function (PSF). These systems are also removed from the sample.

Phase 3 An inclination limit of $i \leq 60^\circ$ is applied to remove highly inclined galaxies as it is difficult to identify if a bar is present in these cases. We define the inclination of a galaxy by measuring the ellipticity of the outermost fitted ellipse,

$$e = 1 - \frac{b}{a}, \quad (1)$$

where b is the minor axis length and a is the major axis length. The inclination is defined as

$$\cos i = \frac{b}{a}. \quad (2)$$

Approximately 8% of the galaxies in the F444W filter of the parent sample were seen to be too highly inclined and were removed from the sample.

Phase	HST		JWST	
	$N_{\text{gal removed}}$	$N_{\text{gal remain}}$	$N_{\text{gal removed}}$	$N_{\text{gal remain}}$
1	4980	465	3635	1583
2	230	235	416	1167
3	102	133	399	768

Table 1. Number of galaxies removed from the sample and the resultant sample size after each optimisation phase. Col. 1: the optimisation phase. Col. 2 and Col. 3 are in the context of HST CANDELS F160W images. Col. 2: the number of galaxies which failed to meet the phase criteria. Col. 3: the sample size after the criteria are applied, with phase 1 being applied to the parent sample. Col. 4 and Col. 5 are the same as Col. 2 and Col. 3 but in the context of JWST CEERS F444W images.

We applied this three-step optimisation procedure to our initial large CEERS F444W galaxy sample, ensuring elliptical isophotes could be fitted to the galaxy image with an identified galactic centre and that the galaxy was not highly inclined. The resultant optimised sample of galaxies suitable to our analysis is 768 CEERS images in the NIRCcam F444W filter (hereafter referred to as the optimised JWST sample). Of the optimised galaxy sample, 393 galaxies are between the redshifts $1 \leq z \leq 2$, and 376 galaxies are between the redshifts $2 < z \leq 3$. Before visual classifications, a co-author (DG) visually verified that all removed objects were indeed poorly resolved, overly faint/irregular, or too inclined. Table 1 gives the number of galaxies removed at each phase and the resultant galaxy sample size.

To measure the difference in the bar fraction between JWST and HST, we also applied the three-step optimisation procedure in our HST CANDELS F160W galaxy sample. This reduced our HST CANDELS sample to an optimised sample of 115 galaxies (hereafter referred to as the optimised HST sample). The poorer sensitivity and wavelength range of HST means many of the galaxies are very pixelated, and features are difficult to discern. Therefore, the ellipse fitting technique failed on many of these galaxies, greatly reducing the optimised HST sample size.

3.2 Disc identification

The fraction of disc galaxies in the optimised JWST sample (f_D) must be calculated to derive the fraction of bars in disc galaxies. Disc galaxies have a distinct exponential radial profile, assisting morphological classifications. Two co-authors (ZLC and DG) visually classified the optimised JWST sample. The participants voted the galaxy to be a disc or non-disc based on the F444W NIRCcam images and a log intensity radial profile. In principle, artefacts (discussed in § 2.1) could mislead visual classifications, but these PSF effects are clearly distinguishable. The diffraction spikes mostly appeared as a large hexagon over the galaxy image, so the galaxy is not elongated in one direction preferentially. Therefore, we typically class these as non-discs/unidentifiable. To ensure we were not affected by less prominent artefacts, we checked for effects in the intensity radial profile of each galaxy. A higher disc fraction is thought to be found in JWST compared to HST due to the improved sensitivity and wavelength range. Figure 2 shows three examples of disc and non-disc galaxies in rest-frame JWST NIRCcam F444W and HST WFC3 F160W filters. Non-disc galaxies can include strong PSF-affected sources, as shown by the central source in the figure. The average disc fraction of the optimised JWST sample is $f_D = 0.40 \pm 0.14$ for the redshift range $1 \leq z \leq 3$. The disc fraction derived in this study agrees with the disc fraction found by LF and collaborators (Ferreira et al. 2022), where six independent participants visually classified 3956 CEERS sources in their rest-frame NIR images, using the fil-

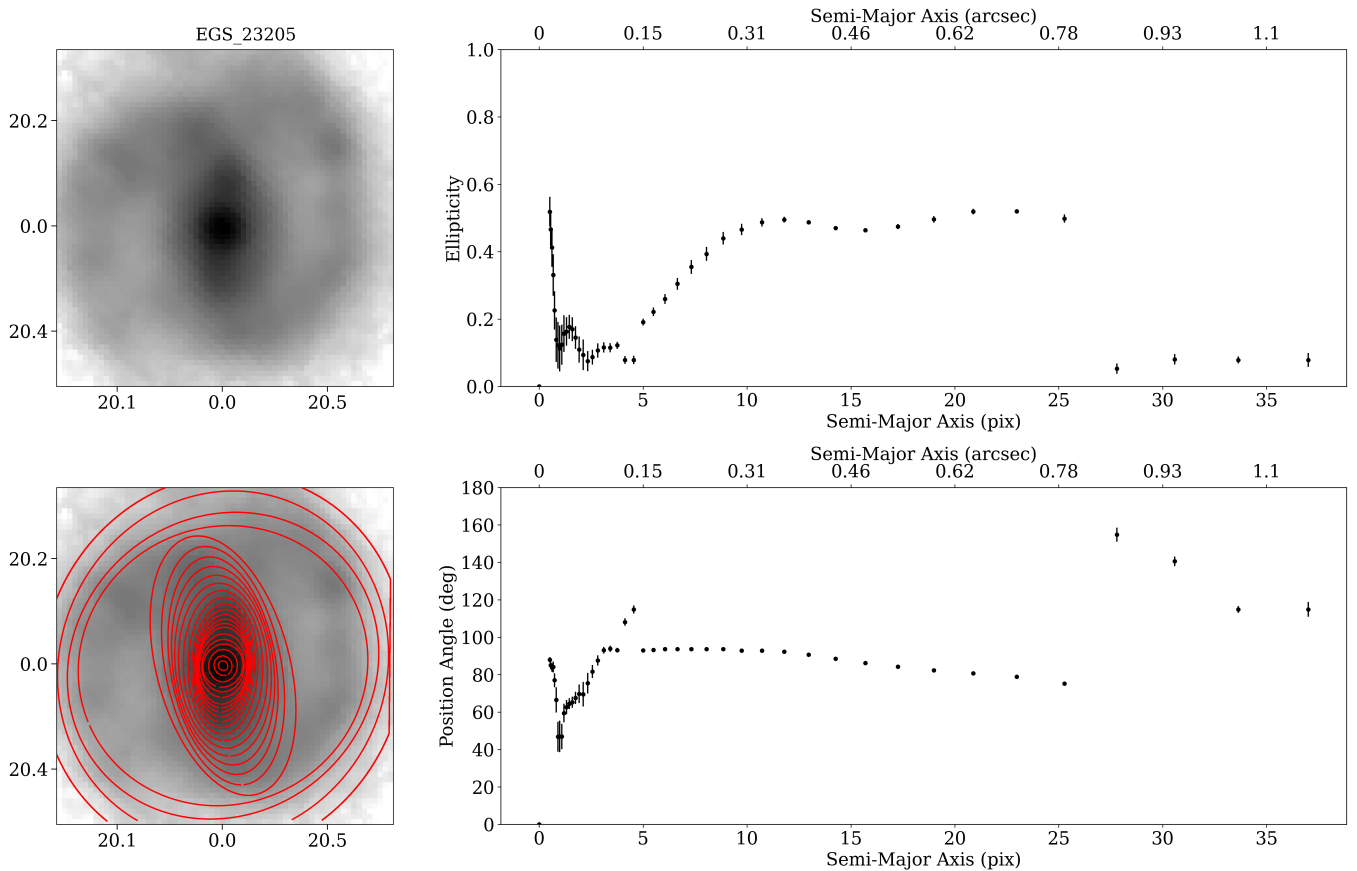


Figure 1. Elliptical isophotal fits using the module `photutils.isophote` from Python’s `astropy` package (Bradley et al. 2022) to logarithmic F444W NIRCcam images of the galaxy EGS_23205 at redshift $z \sim 2.12$. The left-hand side shows the F444W image annotated with the pixel coordinates (top) and superposed elliptical isophotal fits (bottom). The right-hand side shows radial profiles of the ellipticity (e) (top) and position angle (PA) in degrees (bottom) as derived from the ellipse fits.

ters F277W, F356W and F444W for the redshifts $z = 1.5 - 6.5$, which contained 1672 discs, i.e., $f_D \sim 0.42$. Using JWST, Nelson et al. (2023) found that massive, dusty edge-on discs could have been missed as HST-dark galaxies. The systematic error on our f_D , ± 0.14 , is the range of f_D found by the different participants. In § 4, the disc fraction is determined for the redshift bins selected, and the fraction of bars in disc galaxies is thus calculated. For the two redshift bins between $1 \leq z \leq 2$ and $2 < z \leq 3$, 181 and 176 discs were identified, respectively.

3.3 Visual classifications

The optimised JWST sample was then visually classified by five co-authors (ZLC, DG, CdSF, TK and JN). The participants were asked to vote *barred*, *maybe-barred* or *unbarred* on the F444W NIRCcam images. The votes were tallied, and a galaxy was classified as follows: a galaxy is classified as strongly barred if it obtained at least three out of five votes for barred; a galaxy is classified as weakly barred if it obtained two out of five votes for barred or at least three out of five votes for maybe-barred; a galaxy is classified as unbarred if it did not obtain the vote thresholds. Figure 3 is a histogram of the number of barred and maybe-barred votes the co-authors gave on each galaxy in the optimised JWST sample. The figure does not show the galaxies where the co-authors were congruent about the galaxies being unbarred. The figure shows the difficulties in identifying bars

as 75% of the galaxies shown here are below the vote threshold, hence classified as unbarred.

The visual classification method was repeated for the optimised JWST sample in the NIRCcam F356W filter. The resolution marginally improves at this shorter wavelength, so structural features are better defined. However, this wavelength can be more subjected to dust extinction and star formation effects, so the bar-dominated, evolved stellar populations are moderately traced. The overall bar fraction did not change between the two NIRCcam filters, but a few weaker bars became stronger. Finally, the visual classification method was repeated again on the optimised HST sample. The galaxy EGS_31125 is shown in Figure 4 in the three different filters employed: HST WFC3 F160W and JWST NIRCcam F356W and F444W. EGS_31125 is classified in the F444W filter as strongly barred and unbarred in the F160W filter. This figure clearly shows the impact of improved sensitivity and longer wavelength with JWST on the galaxy at redshift $z \approx 2.06$ and how distinctive the disc structures become (see also Guo et al. 2023). On the other hand, it is interesting to note that 15 galaxies have been classified as barred in the HST sample but did not receive any vote when classified using the JWST data. These images were inspected again, and while these galaxies could indeed be barred, we note that in some cases, effects from the JWST PSF impact the classification. In other instances, details in the structure of the galaxy are better discerned in the JWST images, ren-

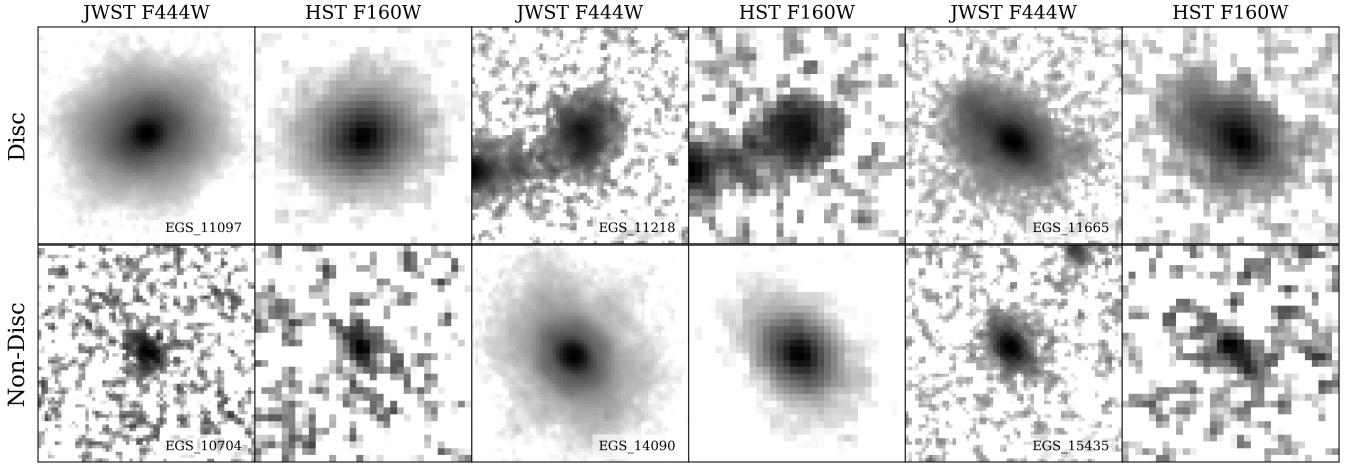


Figure 2. Rest-frame NIR logarithmic images of three disc (top row) and non-disc (bottom row) galaxies. The three exemplars for each classification, with IDs in the lower right of the NIRCам F444W image, are shown in the JWST NIRCам F444W (left) and HST WFC3 F160W (right).

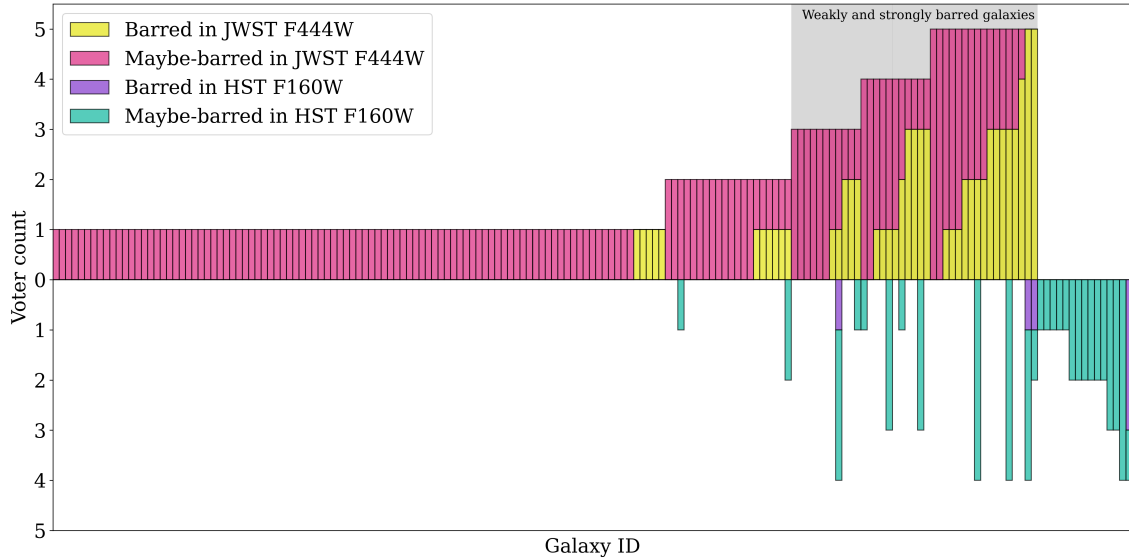


Figure 3. Distribution of the total number of barred in yellow (purple) and maybe-barred in pink (blue) votes cast by the five participating co-authors to candidate galaxies in the optimised JWST (HST) sample. A grey shaded area covers the galaxies which are classified as weakly or strongly barred. We exclude from this figure galaxies that received zero barred or maybe-barred votes.

dering the impression of a bar rather uncertain. We show examples of these galaxies in Figure B1 (Appendix B).

4 THE BAR FRACTION

We aim to determine the fraction of the disc galaxy population at redshifts $z = 1 - 3$ hosting a bar. We visually classified the optimised JWST sample, which met the criteria in § 3.1. The process is repeated for the optimised HST sample to explore if an increase in the bar fraction is found using JWST. Galaxies were classified as described in § 3.3. Figure 5 shows three examples of strongly barred, weakly barred and unbarred galaxies in the JWST NIRCам F444W and HST WFC3 F160W filters. The strongly barred galaxies have distinct stellar structures, while some weakly barred galaxies have less prominent outer discs.

The bar fraction is found for two redshift bins, $1 \leq z \leq 2$ and $2 < z \leq 3$, to observe the evolution of the bar fraction. The redshift was only divided into two bins, as the number of barred galaxies is relatively small. In the optimised JWST sample, 29 galaxies were identified as barred in the lower redshift bin, where eight are strongly barred, and 21 are weakly barred, which decreased to ten barred galaxies in the higher redshift bin, where five are strongly barred, and five are weakly barred. All galaxies classified as barred are shown in Appendix A: Figure A1 shows the strongly barred galaxies, while Figure A2 shows the weakly barred galaxies. In this study, the fraction of barred structures in disc galaxies in the redshift ranges $1 \leq z \leq 2$ and $2 < z \leq 3$ is $\approx 18.9^{+3.6}_{-2.6}$ per cent and $\approx 6.6^{+0.5}_{-0.3}$ per cent, respectively. In the optimised HST sample, nine galaxies were identified as weakly or strongly barred in the lower redshift bin, giving a bar fraction of $\approx 5.9^{+0.5}_{-0.2}$ per cent, and only one weakly barred galaxy was identified in the higher redshift bin, giving a bar

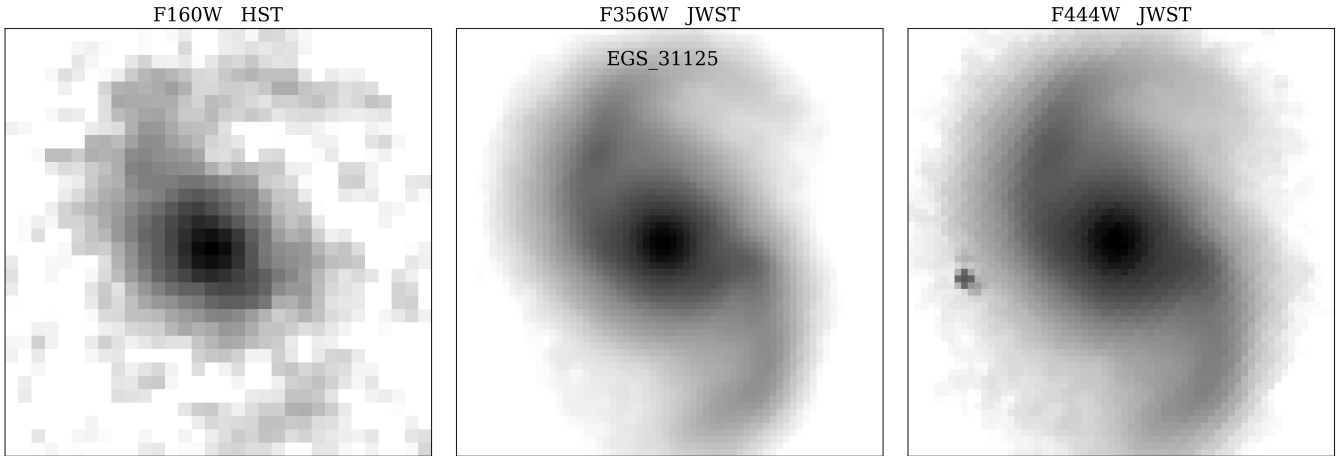


Figure 4. The logarithmic image of galaxy EGS_31125 at redshift $z \approx 2.06$, visually classified as strongly barred from the JWST NIRC2 F444W image, shown in an HST filter and two JWST filters. From left to right: HST WFC3 F160W and JWST NIRC2 F356W and F444W. This filter comparison demonstrates the effects of PSF, sensitivity and wavelength range on a galaxy image, particularly in the context of bars. The image shows EGS_31125 in rest frame 0.52, 1.16, and $1.45 \mu\text{m}$, respectively.

Sample	Redshift	$N_{\text{gal,HST}}$	$N_{\text{gal,JWST}}$	Criteria applied
Total sample	$1 \leq z \leq 6$	7111	7111	N/A
Parent sample	$1 \leq z \leq 3$	5445	5218	Redshift
Optimised sample	$1 \leq z \leq 3$	133	768	ellipse fitting, $i \leq 60^\circ$
	$1 \leq z \leq 2$	108	393	
	$2 < z \leq 3$	25	376	
Disc sample	$1 \leq z \leq 3$	N/A	357	Visually classified discs
	$1 \leq z \leq 2$		181	
	$2 < z \leq 3$		176	
Weakly Barred	$1 \leq z \leq 3$	9	26	Visually classified bars
	$1 \leq z \leq 2$	8	21	
	$2 < z \leq 3$	1	5	
Strongly Barred	$1 \leq z \leq 3$	1	13	Visually classified bars
	$1 \leq z \leq 2$	1	8	
	$2 < z \leq 3$	0	5	

Table 2. Progression of the galaxy samples after the different selection and classification criteria are applied. Col. (1): the sample label. Col. (2): the redshift range. Col. (3): the number of galaxies after applying the criteria to HST CANDELS F160W images. Col. (4): the number of galaxies after applying the criteria to JWST CEERS F444W images. Col. (5): the criteria applied.

fraction of $\approx 0.7^{+0.001}_{-2.7e-5}$ per cent. The uncertainties quoted are the 1σ Bayesian binomial confidence intervals (Cameron 2011), and their derivation is explained below. Table 2 shows the progression of the JWST and HST galaxy samples after the different selection and classification criteria are applied.

Figure 6 shows the visually classified bar fraction versus redshift and lookback time in the context of other observational work assessing strong bar fractions using HST. The figure shows that previous results based on HST data indicate a decline in the bar fraction from lower to higher redshifts. While the JWST bar fraction also decreases from the redshift bin $1 \leq z \leq 2$ to the redshift bin $2 < z \leq 3$, the JWST bar fraction in the lower redshift bin is more than three times the HST bar fraction in the same redshift bin. Therefore, our results clearly show that the bar fraction is significantly higher than what could be found with HST data. A dashed line indicates the redshift range of our visually identified barred galaxies, and a thick solid line indicates the distribution quartiles, i.e. 25%-75%. We identify the highest redshift strongly barred galaxy as EGS_24268 at $z \approx 2.32$ (also found in Guo et al. 2023) and the highest redshift weakly barred galaxy as EGS_22729 at $z \approx 2.82$.

The higher redshift bin HST bar fraction is close to zero, and thus, a Bayesian approach is used to determine the statistical uncertainty in the computed bar fractions. Considering the fraction of a large population with a given attribute (i.e., bars) and neither close to 0 nor 1, the Normal approximation can be assumed to derive uncertainties, but for small sample sizes and extreme population proportion values (e.g., the HST bar fraction at $2 < z \leq 3$), Cameron (2011) convincingly argues for a Bayesian approach to binomial confidence intervals. We adopt this method to estimate the full 68 per cent confidence intervals described above of the bar fraction in the two redshift bins. The sample used in this study is approximately mass complete (see below), meaning we do not account for incomplete sampling in the uncertainty estimates. On the other hand, the more important systematic errors in our analysis stem from the difficulty of defining a galaxy as a disc or barred galaxy. The fraction of disc galaxies was estimated by taking the average of the fractions determined above. The range of these two independent fractions is interpreted as the main systematic error in the bar fractions. For $1 \leq z \leq 2$ and $2 < z \leq 3$, the difference between the participants' disc fractions is 9.0 and 5.1 per cent, respectively. Hence, the sum in quadrature of the systematic

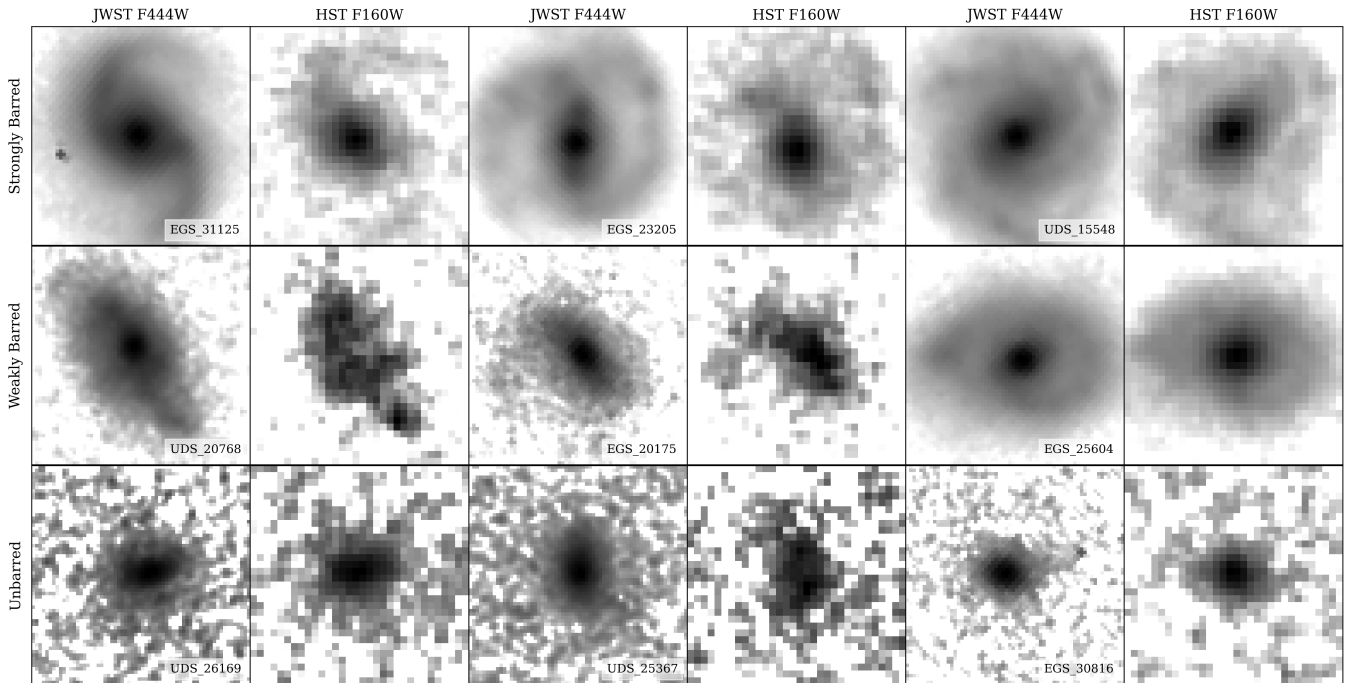


Figure 5. Rest-frame NIR logarithmic images of three strongly barred (top row), weakly barred (middle row) and unbarred (bottom row) galaxies. The three exemplars for each classification, with IDs in the lower right of the NIRCам F444W image, are shown in the JWST NIRCам F444W (left) and HST WFC3 F160W (right).

and statistical errors of the JWST bar fractions are $\approx 18.9^{+9.7}_{-9.4}$ per cent and $\approx 6.6^{+7.1}_{-5.9}$ per cent.

In Figure 7, we show the distribution of stellar mass as a function of redshift for all disc galaxies in the optimised sample. The disc galaxies are taken from the classification of one of the participants in the disc classification procedure (ZLC). Still, we verified that qualitatively similar results are found regardless of the classifier. The 95% empirical completeness limit of the sample, as estimated in Duncan et al. (2019), is indicated, showing that most of our sample is above or close to the completeness limit. Interestingly, this figure shows that barred galaxies tend to avoid the least massive galaxies at each redshift, in line with the results from Sheth et al. (2008).

5 DISCUSSION

Using NIRCам F444W images, corresponding to NIR rest-frame at $1 \leq z \leq 3$, the visually identified fraction of disc galaxies hosting a bar at redshifts $z = 1-2$ is ~ 20 per cent, which decreases to ~ 10 per cent at redshifts $z = 2-3$. We found the bar fraction obtained from the F444W JWST images to be about three to four times greater than the bar fraction obtained using F160W HST images, as shown in Figure 6. In fact, the value of the bar fraction at $z = 1-2$, that we derive using HST images, matches perfectly the estimate from Simmons et al. (2014, see their Fig. 6) who also use HST data for their estimates. This begs the question, why do we find more bars in JWST than in HST images? Considering that the parent sample was chosen to contain sources present in both HST CANDELS and JWST CEERS and that the same bar-detection method was applied to both the JWST F444W and HST F160W images, the considerable difference between the JWST and HST bar fractions at each redshift bin implies that the identification of bars in disc galaxies is dependent on the sensitivity

and wavelength range of the instrument; the bar fraction increases at longer wavelengths and with improved sensitivity. Defining the resolution of an instrument as the full-width half maximum (FWHM) of the empirical point spread function (PSF), the resolution of HST at $1.6 \mu\text{m}$ is $0.151''^3$ and the resolution of JWST at $4.44 \mu\text{m}$ is $0.145''^4$, and therefore, our result do not give insight into the bar fraction dependence on resolution.

Our results build upon the previous studies, which find that bar-driven internal evolutionary processes for settled disc populations begin at $z \approx 1$, whereas our new results suggest this to be $z \approx 2$. Additionally, our study finds that a sizable population of barred galaxies exists at $z \leq 3$, implying that massive disc galaxies can become dynamically settled with prominent bars at a lookback time of ~ 11 Gyrs. The idea that bar-driven galaxy evolution happens at $z > 2$ is generally consistent with the early bar formation epochs estimated for local galaxies in the Time Inference with MUSE in Extragalactic Rings (TIMER) project (Gadotti et al. 2019). For NGC 4371, it has been estimated that the bar formation happened at $z \approx 2$ (Gadotti et al. 2015), while for NGC 1433, this happened at $z \approx 1$ (de Sá-Freitas et al. 2023). Nonetheless, it is important to point out that not necessarily all barred galaxies observed at $2 < z \leq 3$ will remain as a barred disc galaxy down to $z \approx 0$, as the galaxies in the TIMER sample: late violent mergers may destroy the bar, as well as the disc altogether.

³ PSF FWHM taken from the HST user documentation: <https://hst-docs.stsci.edu/wfc3ihb/chapter-7-ir-imaging-with-wfc3/7-6-ir-optical-performance>

⁴ PSF FWHM taken from the JWST user documentation: <https://jwst-docs.stsci.edu/jwst-near-infrared-camera/nircam-performance/nircam-point-spread-functions>

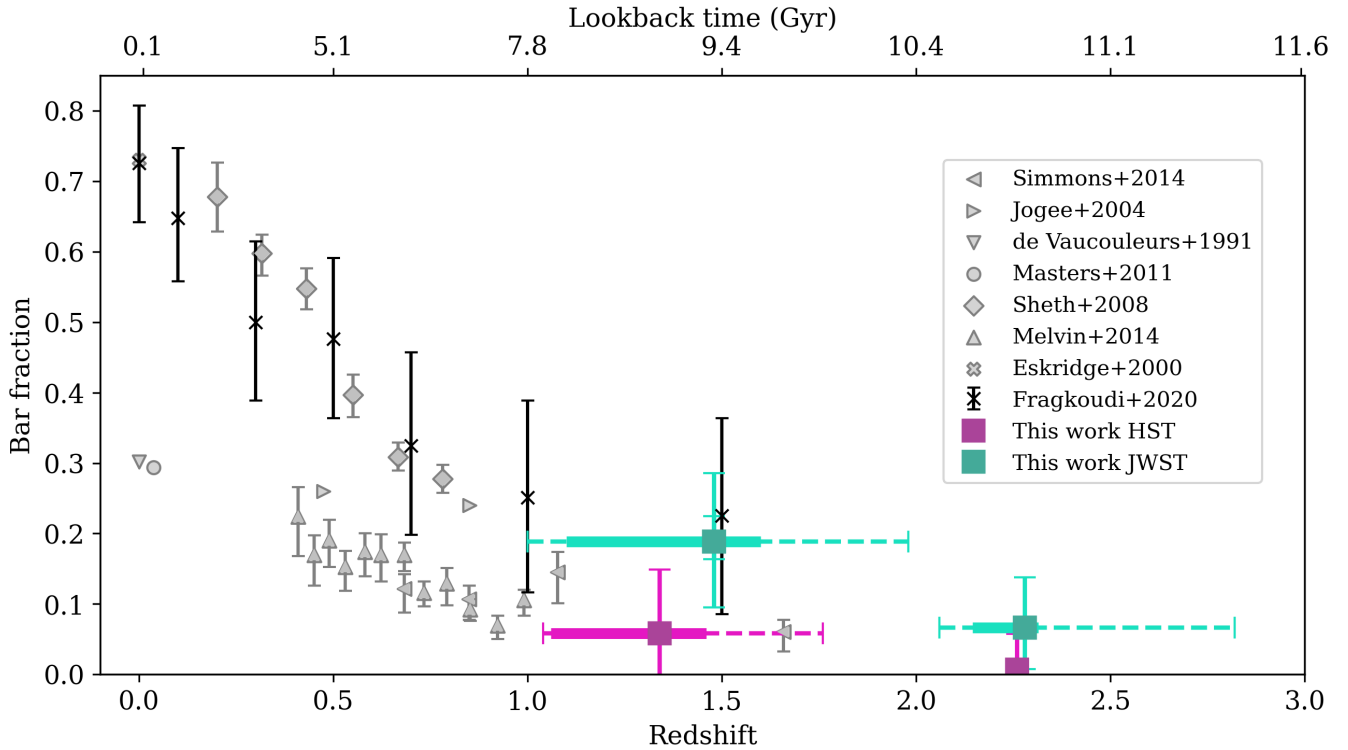


Figure 6. Evolution of the fraction of stellar bars in disc galaxies with redshift in the context of other bar assessment work using HST. The fractions of barred disc galaxies found in JWST NIRCcam images are shown as green squares, and the fractions of barred disc galaxies found in this study in HST WFC3 images are shown as purple squares. The bar fraction was found for two redshift bins, $1 \leq z \leq 2$ and $2 < z \leq 3$, where the marker indicates the median redshift of the barred galaxies. All bar fraction errors indicate the sum in quadrature of the systematic and 1σ Bayesian binomial confidence interval (Cameron 2011, statistical error only in dark colours). A dashed line indicates the redshift range of barred galaxies. A thick solid line indicates the redshift range of the quartiles 25%-75% of the distribution of barred galaxies. At low redshifts, de Vaucouleurs et al. (1991, down-pointing triangle) and Masters et al. (2011, circle) found strong bars in a third of disc galaxies, while Eskridge et al. (2000, cross) found strong and weak bars in over two-thirds of disc galaxies. Simmons et al. (2014, left-pointing triangles), Sheth et al. (2008, diamonds) and Melvin et al. (2014, up-pointing triangles) found a decreasing trend of the bar fraction for higher redshifts. Jogee et al. (2004, right-pointing triangles) found a minimal decline in the bar fraction at higher redshifts. Finally, the bar fractions, as found in the Auriga cosmological simulations in Fragkoudi et al. (2020, exes) are shown in black.

In a recent study conducted by Guo et al. (2023), six strongly barred galaxies were identified at $z > 1$ using rest-frame NIR images from the first four pointings of CEERS. The six observed galaxies have a range in redshift from $z \approx 1.1$ to $z \approx 2.3$, using photometric redshifts (see Guo et al. 2023; Stefanon et al. 2017). In a cross-check, we find that all barred galaxies identified by Guo et al. were also classified by us as barred.

Several previous studies have found a decline in the fraction of bars in disc and spiral galaxies with redshift, however mass- and volume-limits vary between the studies, along with the bar classification method. Sheth et al. (2008) observe the evolution of the bar fraction at redshifts $0.2 < z < 0.84$ from luminous (brighter than L_V^*) face-on spiral galaxies in the COSMOS 2 deg^2 field. The classification methods used in Sheth et al. are ellipse-fitting and visual, which are cross-checked, and an agreement of 85% is found. Masters et al. (2011) found the bar fraction of a volume-limited visually selected SDSS sample using Galaxy Zoo at redshifts $0.01 < z < 0.06$ and $M_r < -19.38$. Melvin et al. (2014) use visually selected galaxies via Galaxy Zoo from COSMOS HST images at redshifts $0.4 \leq z \leq 1.0$ with an applied stellar mass limit of $\log(M_*/M_\odot) \geq 10$. The bar fraction was extended to redshifts $0.5 \leq z \leq 2.0$ in Simmons et al. (2014) through the visually selected CANDELS galaxies via Galaxy

Zoo with an absolute H -band magnitude limit of $H < 25.5$. With the work of Simmons et al. overlapping with the lower redshift bin of our study and using visually identified CANDELS galaxies, we found that our results are in full agreement. Although many studies have found a decrease in the bar fraction at $z = 0 - 1$, some find little or no evolution of the bar fraction. Jogee et al. (2004) identified bars in spiral galaxies using three independent techniques and found the fraction of bars to be $\sim 30 \pm 6$ per cent in COSMOS-ACS galaxies at redshifts $z \sim 0.2 - 0.7$ and $z \sim 0.7 - 1.0$, with completeness cuts of $M_V \leq -19.3$ and -20.6 , respectively. Elmegreen et al. (2004) also found a constant bar fraction of $\sim 23 \pm 3$ per cent at redshifts $z \sim 0.0 - 1.0$ in COSMOS-ACS galaxies.

A direct comparison between the results from these various studies is difficult to accomplish given the different techniques employed to identify bars and the different sample selection criteria. In particular, Erwin (2018) shows that in the local Universe the bar fraction depends strongly on galaxy mass, with a peak at $M_* \sim 10^{9.7} M_\odot$, declining towards both higher and lower masses. At redshifts $0.2 \leq z \leq 0.6$ for a mass complete sample of $M > 10^{10.5} M_\odot$ galaxies in the COSMOS field, Cameron et al. (2010) found the bar fraction of early-type discs with intermediate stellar masses to be twice that of late-type discs, and is reversed for high stellar masses. In this context, it is important to highlight that our sample probes the galaxy population with masses

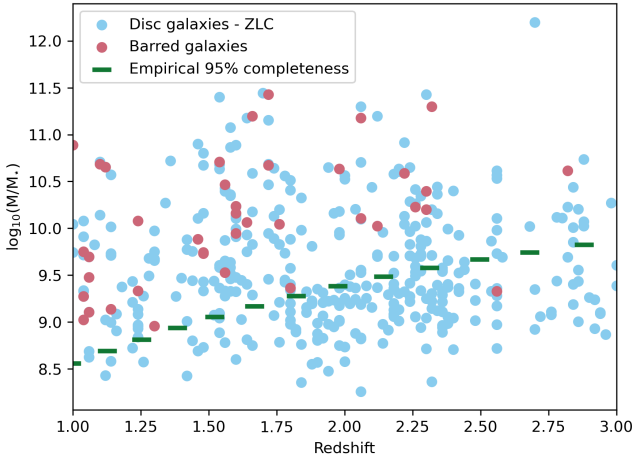


Figure 7. Distribution of stellar masses for the sample of disc galaxies as classified by ZLC in JWST CEERS between the redshifts $1 \leq z \leq 3$. Disc galaxies are shown in blue, while the weakly and strongly barred galaxies are in pink. A dashed green line shows the 95% empirical completeness of the sample (see Figure 8 of [Duncan et al. 2019](#)). The parameter space below this line in this plot corresponds to a completeness fraction of $\approx 85 - 90\%$.

above $\approx 10^9 M_\odot$, which at redshift zero may reflect the peak in the bar fraction distribution. Considering all barred galaxies we find in our study, their mean stellar mass is $M_\star \sim 1.2 \times 10^{10} M_\odot$, with a standard deviation of $\sim 5.8 \times 10^{10} M_\odot$.

Using the magnetic-hydrodynamical cosmological simulation TNG50 ([Nelson et al. 2019](#)), [Rosas-Guevara et al. \(2022\)](#) found that $M_\star \geq 10^{10} M_\odot$ spiral galaxies with bar formation are present as early as $z = 4$. When an angular resolution limit of twice the HST *I*-band angular PSF FWHM was applied, the fraction of bars dropped to a tenth of its original value at $z = 2$, reconciling theoretical predictions and observations.

Some of the previous observational studies discussed above suggest that the decrease in the bar fraction in massive disc galaxies out to $z \sim 1$ could be due to minor merger events that keep the disc dynamically hot. However, depending on the details of the merger/flyby interaction, this could, in fact, tidally induce bar formation (e.g., [Berentzen et al. 2003](#); [Peschken & Lokas 2019](#)).

The decline in the bar fraction in disc galaxies could be explained as a result of the decreasing physical spatial resolution with redshift. The ellipticity of bars at poorer resolution decreases, leading to a rounder, less elongated and compact bar, making the stellar bar less distinguishable. The perceptibility of a bar could be considerably affected by a clumpy outer disc, a bright central bulge and/or the angular size of the bar (e.g., [Lee et al. 2019](#)). In the context of our results using JWST, the PSF FWHM for the JWST F444W filter is $0.145''$. The median redshift for barred galaxies between $1 \leq z \leq 2$ is $z = 1.48$, corresponding to a mean linear resolution of ≈ 1.26 kpc. As for the redshift bin $2 < z \leq 3$, the median redshift of barred galaxies is $z = 2.28$, corresponding to a mean linear resolution of ≈ 1.22 kpc. Bars smaller in angular size could have been preferentially missed at the high redshifts explored in this study. In a volume-limited SDSS galaxy sample where bars were identified through ellipse fits and Fourier analysis, [Aguerri et al. \(2009\)](#) established that only bars with lengths above 2.5 times the FWHM can be identified. The proposal that the high-redshift bar fraction is systematically underestimated was thoroughly discussed in the context of a mass- and volume-limited S^4G galaxy sample in [Erwin \(2018\)](#).

Erwin successfully reproduced SDSS bar fraction trends using SDSS observational parameters in simulations on the S^4G galaxy sample and suggested a bar length detection limit of ~ 2 times the FWHM. Applying these detection limits on NIRCам F444W images implies that bars shorter than $\sim 2.5 - 3$ kpc in radius (semi-major axis) are missed in our study.

Our resolution limit thus indicates that all bars we detect in this study are longer than ≈ 3 kpc and then presumably relatively strong bars. In this context, it is striking that the bar fraction we estimate at the redshift bin $z = 1 - 2$ is not too dissimilar to the local strong bar fraction of about 30% (e.g., [de Vaucouleurs et al. 1991](#)). In fact, [Erwin \(2005\)](#) found that the mean bar semi-major axis is 3.3 kpc for early-type disc galaxies and 1.5 kpc for late-type disc galaxies (see also [Gadotti 2011](#)). Therefore, unless the bar size distribution at high redshifts differs from the local distribution, even with JWST, we are likely missing a sizeable fraction of barred galaxies. In a sample of massive galaxies ($M_\star \geq 10^{10} M_\odot$, $0.02 \leq z \leq 0.07$) studied in [Gadotti \(2011\)](#), there are not many bars that are shorter than 3 kpc (see his Fig. 1) although the author points out that due to resolution limits, he may also miss bars with semi-major axis below 2 – 3 kpc. However, in [Erwin \(2005\)](#), mass is not presented, so a direct comparison is not straightforward. [Erwin \(2019\)](#), on the other hand, shows that bar length increases with mass for galaxies more massive than $\log(M_\star/M_\odot) \leq 10.1$ for local galaxies, and a substantial fraction of the galaxies in his study has bars shorter than 3 kpc.

Not only absolute bar length but the ratio of bar length to the galaxy size (e.g., disk scale length h , or parameters such as R_{50} or R_{90}) may be more useful to compare at different redshifts, since it has been shown that the galaxy size also evolves ([Trujillo et al. 2007](#); [Buitrago et al. 2008](#); [van der Wel et al. 2014](#); [Buitrago et al. 2014](#); [Whitney et al. 2019](#), mostly for massive early-type galaxies but also in the case of disk galaxies). [Kim et al. \(2021\)](#) measured bar length for galaxies at $0.2 \leq z \leq 0.84$ and found that the mean length of the bar is ~ 5 kpc for galaxies with $\log(M_\star/M_\odot) \geq 10$ (see their Fig. 2). However, the normalised bar length R_{bar}/h of galaxies at $0.2 \leq z \leq 0.84$ in the study of [Kim et al. \(2021\)](#) is similar to that of local bars in [Gadotti \(2011\)](#). We postpone a thorough discussion on these aspects to a future paper, in which we will also present measurements of the bar length and its evolution at higher redshifts.

6 SUMMARY AND CONCLUSIONS

To derive the fraction of stellar bars in disc galaxies at high redshifts is an essential step towards understanding the onset of bar-driven galaxy evolution, which was found in previous studies using rest-frame optical HST images to occur at $z \sim 1$. However, stellar bars are populated by evolved stars emitting strongly at longer wavelengths, and thus, bars can be more effectively identified in rest-frame NIR images.

In this study, we observe the evolution of the bar fraction at redshifts $z = 1 - 3$ in a sample of galaxies present in both HST CANDELS and JWST CEERS and PRIMER and compare the results obtained after using rest-frame optical HST images and rest-frame NIR JWST images for galaxies in the same parent sample. We use the longest-wavelength JWST NIRCам F444W filter to trace the underlying stellar mass distribution as best as possible. The initial parent sample of 5241 galaxies is optimised to produce a sample in which bars can be more robustly identified, in particular by removing galaxies in a close to edge-on projection, with an inclination limit of $i \leq 60^\circ$. After optimisation, the parent sample is reduced to 768 galaxies in

the JWST F444W filter and 115 galaxies in the HST F160W filter. Five co-authors visually classified all galaxies in the two optimised samples, searching for bars supported by radial profiles of isophotal ellipticity and position angle.

Two co-authors visually classified all galaxies in the optimised JWST samples as disc or non-disc galaxies and found a disc fraction $f_D \sim 0.40 \pm 0.14$. The fraction of bars in disc galaxies was thus derived for two redshift bins, $1 \leq z \leq 2$ and $2 < z \leq 3$, with robust photometric redshifts. The bar fractions we found in JWST F444W are, respectively, $\approx 19\%$ and $\approx 7\%$ for the lower and higher redshift bins. In HST F160W, we found the bar fractions to be $\approx 6\%$ and $\approx 1\%$ for the lower and higher redshift bins, respectively. We thus found the bar fraction to be approximately three to four times greater in JWST F444W than in HST F160W in the lower redshift bin, showing that the detectability of stellar bars depends greatly on the wavelength range and the sensitivity of the instrument. A decrease in the bar fraction is observed at higher redshifts, but the trend could be due to shorter bars being preferentially missed from this study. We detect a substantial number of barred galaxies at redshifts $z \leq 3$, implying that bar-driven galaxy evolution commences at a lookback time beyond ~ 11 Gyrs. In fact, Guo et al. (2023) have recently reported the finding of a barred galaxy at $z \approx 2.3$, and other teams have reported candidate barred galaxies beyond redshift three (Amvrosiadis et al. 2023, subm.) and even beyond redshift four (Tsukui et al. 2023; Smail et al. 2023). In this study, the highest redshift strongly and weakly barred galaxies found are at $z \approx 2.3$ and $z \approx 2.8$, respectively.

This study does not extend beyond $z = 3$ to remain in the rest-frame NIR and better detect the evolved stellar populations within the bar. Interesting investigations can be done on the bar fraction dependence on galaxy stellar mass and the evolution of the bar length, which are beyond the scope of this paper but will be explored in future papers. This study used the first four pointing of CEERS, and a future paper will present an enlarged census of the bar fraction at redshifts $1 \leq z \leq 3$ using the additional six CEERS pointings.

ACKNOWLEDGEMENTS

ZLC acknowledges funding from the Science and Technology Facilities Council ST/X508354/1. This work was supported by STFC grants ST/T000244/1 and ST/X001075/1. TK acknowledges support from the Basic Science Research Program through the National Research Foundation of Korea (NRF), funded by the Ministry of Education (RS-2023-00240212 and No. 2019R1I1A3A02062242) and the grant funded by the Korean government (MSIT) (No. 2022R1A4A3031306 and WISET 2022-804). JN acknowledges funding from the European Research Council (ERC) under the European Union's Horizon 2020 research and innovation programme (grant agreement No. 694343). EA thanks the CNES for financial support. For the purpose of open access, the authors have applied a Creative Commons Attribution (CC BY) to any Author Accepted Manuscript version arising.

DATA AVAILABILITY

This work used Astropy (Astropy Collaboration et al. 2013) and PHOTUTILS (Bradley et al. 2022). The specific observations analyzed can be accessed via <https://doi.org/10.17909/xm8m-tt59>, and the visual classifications from Ferreira et al. (2022) are publicly available at https://github.com/astroferreira/CEERS_EPOCHS_MORPHO/

REFERENCES

- Abraham R. G., Merrifield M. R., Ellis R. S., Tanvir N. R., Brinchmann J., 1999, *MNRAS*, **308**, 569
- Abraham S., Aniyani A. K., Kembhavi A. K., Philip N. S., Vaghmare K., 2018, *MNRAS*, **477**, 894
- Adams N. J., et al., 2023, *MNRAS*, **518**, 4755
- Aguerre J. A. L., Méndez-Abreu J., Corsini E. M., 2009, *A&A*, **495**, 491
- Allard E. L., Knapen J. H., Peletier R. F., Sarzi M., 2006, *MNRAS*, **371**, 1087
- Alonso M. S., Coldwell G., Lambas D. G., 2013, *A&A*, **549**, A141
- Alonso S., Coldwell G., Duplancic F., Mesa V., Lambas D. G., 2018, *A&A*, **618**, A149
- Astropy Collaboration et al., 2013, *A&A*, **558**, A33
- Athanassoula E., 1992, *MNRAS*, **259**, 345
- Athanassoula L., 2003, Angular Momentum Redistribution and the Evolution and Morphology of Bars. Springer Berlin Heidelberg, Berlin, Heidelberg, pp 313–326, doi:10.1007/978-3-540-45040-5_26, https://doi.org/10.1007/978-3-540-45040-5_26
- Athanassoula E., 2005, *Celestial Mechanics and Dynamical Astronomy*, **91**, 9
- Athanassoula E., Morin S., Wozniak H., Puy D., Pierce M. J., Lombard J., Bosma A., 1990, *MNRAS*, **245**, 130
- Athanassoula E., Rodionov S. A., Peschken N., Lambert J. C., 2016, *ApJ*, **821**, 90
- Barazza F. D., Jogee S., Marinova I., 2008, *ApJ*, **675**, 1194
- Barazza F. D., et al., 2009, *A&A*, **497**, 713
- Berentzen I., Athanassoula E., Heller C. H., Fricke K. J., 2003, *MNRAS*, **341**, 343
- Bittner A., et al., 2020, *A&A*, **643**, A65
- Bradley L., et al., 2022, astropy/photutils: 1.5.0, doi:10.5281/zenodo.6825092, <https://doi.org/10.5281/zenodo.6825092>
- Buitrago F., Trujillo I., Conselice C. J., Bouwens R. J., Dickinson M., Yan H., 2008, *ApJ*, **687**, L61
- Buitrago F., Conselice C. J., Epinat B., Bedregal A. G., Grützbauch R., Weiner B. J., 2014, *MNRAS*, **439**, 1494
- Buta R., Alpert A. J., Cobb M. L., Crocker D. A., Purcell G. B., 1998, *AJ*, **116**, 1142
- Buta R. J., et al., 2015, *ApJS*, **217**, 32
- Cameron E., 2011, *Publ. Astron. Soc. Australia*, **28**, 128
- Cameron E., et al., 2010, *MNRAS*, **409**, 346
- Carles C., Martel H., Ellison S. L., Kawata D., 2016, *MNRAS*, **463**, 1074
- Cheng T.-Y., Huertas-Company M., Conselice C. J., Aragón-Salamanca A., Robertson B. E., Ramachandra N., 2021, *MNRAS*, **503**, 4446
- Cheung E., et al., 2013, *ApJ*, **779**, 162
- Cisternas M., Sheth K., Salvato M., Knapen J. H., Civano F., Santini P., 2015, *ApJ*, **802**, 137
- Coelho P., Gadotti D. A., 2011, *ApJ*, **743**, L13
- Combes F., Sanders R. H., 1981, *A&A*, **96**, 164
- Combes F., Debbasch F., Friedli D., Pfenniger D., 1990, *A&A*, **233**, 82
- Contopoulos G., Grosbol P., 1989, *A&ARv*, **1**, 261
- Contopoulos G., Papayannopoulos T., 1980, *A&A*, **92**, 33
- Di Matteo P., Haywood M., Combes F., Semelin B., Snaith O. N., 2013, *A&A*, **553**, A102
- Duncan K., et al., 2019, *ApJ*, **876**, 110
- Dunlop J. S., et al., 2021, PRIMER: Public Release IMaging for Extragalactic Research, JWST Proposal. Cycle 1, ID. #1837
- Elmegreen B. G., Elmegreen D. M., Hirst A. C., 2004, *ApJ*, **612**, 191
- Erwin P., 2005, *MNRAS*, **364**, 283
- Erwin P., 2018, *MNRAS*, **474**, 5372
- Erwin P., 2019, *MNRAS*, **489**, 3553
- Eskridge P. B., et al., 2000, *AJ*, **119**, 536
- Ferreira L., et al., 2022, *arXiv e-prints*, p. arXiv:2210.01110
- Finkelstein S. L., et al., 2023, *ApJ*, **946**, L13
- Fragkoudi F., Athanassoula E., Bosma A., 2016, *MNRAS*, **462**, L41
- Fragkoudi F., Di Matteo P., Haywood M., Schultheis M., Khoperskov S., Gómez A., Combes F., 2018, *A&A*, **616**, A180
- Fragkoudi F., et al., 2020, *MNRAS*, **494**, 5936

- Frogel J. A., Quillen A. C., Pogge R. W., 1996, in Block D. L., Greenberg J. M., eds, *Astrophysics and Space Science Library* Vol. 209, New Extragalactic Perspectives in the New South Africa. p. 65, doi:10.1007/978-94-009-0335-7_7
- Gadotti D. A., 2011, *MNRAS*, **415**, 3308
- Gadotti D. A., Athanassoula E., Carrasco L., Bosma A., de Souza R. E., Recillas E., 2007, *MNRAS*, **381**, 943
- Gadotti D. A., Seidel M. K., Sánchez-Blázquez P., Falcón-Barroso J., Husemann B., Coelho P., Pérez I., 2015, *A&A*, **584**, A90
- Gadotti D. A., et al., 2019, *MNRAS*, **482**, 506
- Gadotti D. A., et al., 2020, *A&A*, **643**, A14
- Garland I. L., et al., 2023, *MNRAS*, **522**, 211
- Grogin N. A., et al., 2011, *ApJS*, **197**, 35
- Guo Y., et al., 2023, *ApJ*, **945**, L10
- Hohl F., 1971, *ApJ*, **168**, 343
- Huertas-Company M., et al., 2023, *arXiv e-prints*, p. arXiv:2305.02478
- Ishizuki S., Kawabe R., Ishiguro M., Okumura S. K., Morita K.-I., 1990, *Nature*, **344**, 224
- Jedrzejewski R. I., 1987, *MNRAS*, **226**, 747
- Jogee S., et al., 2004, *ApJ*, **615**, L105
- Kalnajs A. J., 1972, *ApJ*, **175**, 63
- Kim T., Athanassoula E., Sheth K., Bosma A., Park M.-G., Lee Y. H., Ann H. B., 2021, *ApJ*, **922**, 196
- Knapen J. H., Beckman J. E., Heller C. H., Shlosman I., de Jong R. S., 1995, *ApJ*, **454**, 623
- Koekemoer A. M., et al., 2011, *ApJS*, **197**, 36
- Kormendy J., 1982, *ApJ*, **257**, 75
- Kormendy J., Kennicutt Robert C. J., 2004, *ARA&A*, **42**, 603
- Kraljic K., Bournaud F., Martig M., 2012, *ApJ*, **757**, 60
- Lee Y. H., Ann H. B., Park M.-G., 2019, *ApJ*, **872**, 97
- Lynden-Bell D., Kalnajs A. J., 1972, *MNRAS*, **157**, 1
- Marinova I., Jogee S., 2007, *ApJ*, **659**, 1176
- Masters K. L., et al., 2011, *MNRAS*, **411**, 2026
- Melvin T., et al., 2014, *MNRAS*, **438**, 2882
- Menéndez-Delmestre K., Sheth K., Schinnerer E., Jarrett T. H., Scoville N. Z., 2007, *ApJ*, **657**, 790
- Nair P. B., Abraham R. G., 2010, *ApJ*, **714**, L260
- Nelson D., et al., 2019, *Computational Astrophysics and Cosmology*, **6**, 2
- Nelson E. J., et al., 2023, *The Astrophysical Journal Letters*, **948**, L18
- Ostriker J. P., Peebles P. J. E., 1973, *ApJ*, **186**, 467
- Peschken N., Lokas E. L., 2019, *MNRAS*, **483**, 2721
- Planck Collaboration et al., 2020, *A&A*, **641**, A6
- Regan M. W., et al., 2006, *ApJ*, **652**, 1112
- Rosas-Guevara Y., et al., 2022, *MNRAS*, **512**, 5339
- Sakamoto K., Okumura S. K., Ishizuki S., Scoville N. Z., 1999, *ApJ*, **525**, 691
- Sanders R. H., Tubbs A. D., 1980, *ApJ*, **235**, 803
- Schneider P., 2006, *Extragalactic Astronomy and Cosmology*. Springer Berlin, Heidelberg
- Sellwood J. A., Wilkinson A., 1993, *Reports on Progress in Physics*, **56**, 173
- Sheth K., Regan M. W., Scoville N. Z., Strubbe L. E., 2003, *ApJ*, **592**, L13
- Sheth K., Vogel S. N., Regan M. W., Thornley M. D., Teuben P. J., 2005, *ApJ*, **632**, 217
- Sheth K., et al., 2008, *ApJ*, **675**, 1141
- Silva-Lima L. A., Martins L. P., Coelho P. R. T., Gadotti D. A., 2022, *A&A*, **661**, A105
- Simmons B. D., et al., 2014, *MNRAS*, **445**, 3466
- Smail I., et al., 2023, Hidden giants in JWST's PEARLS: An ultra-massive $z=4.26$ sub-millimeter galaxy that is invisible to HST (arXiv:2306.16039)
- Stefanon M., et al., 2017, *ApJS*, **229**, 32
- Trujillo I., Conselice C. J., Bundy K., Cooper M. C., Eisenhardt P., Ellis R. S., 2007, *MNRAS*, **382**, 109
- Tsukui T., Wisnioski E., Bland-Hawthorn J., Mai Y., Iguchi S., Baba J., Freeman K., 2023, Detecting a disk bending wave in a barred-spiral galaxy at redshift 4.4 (arXiv:2308.14798)
- Wang Y., Athanassoula E., Patsis P., Mao S., 2022, *A&A*, **668**, A55
- Weinberg M. D., 1985, *MNRAS*, **213**, 451
- Whitney A., Conselice C. J., Bhatawdekar R., Duncan K., 2019, *ApJ*, **887**, 113
- Wozniak H., Friedli D., Martinet L., Martin P., Bratschi P., 1995, *A&AS*, **111**, 115
- Wright E. L., 2006, *PASP*, **118**, 1711
- de Lorenzo-Cáceres A., Vazdekis A., Aguerri J. A. L., Corsini E. M., Debatista V. P., 2012, *MNRAS*, **420**, 1092
- de Sá-Freitas C., et al., 2023, *A&A*, **671**, A8
- de Vaucouleurs G., de Vaucouleurs A., Corwin Herold G. J., Buta R. J., Paturel G., Fouque P., 1991, *Third Reference Catalogue of Bright Galaxies*. Springer-Verlag
- van der Wel A., et al., 2014, *ApJ*, **788**, 28

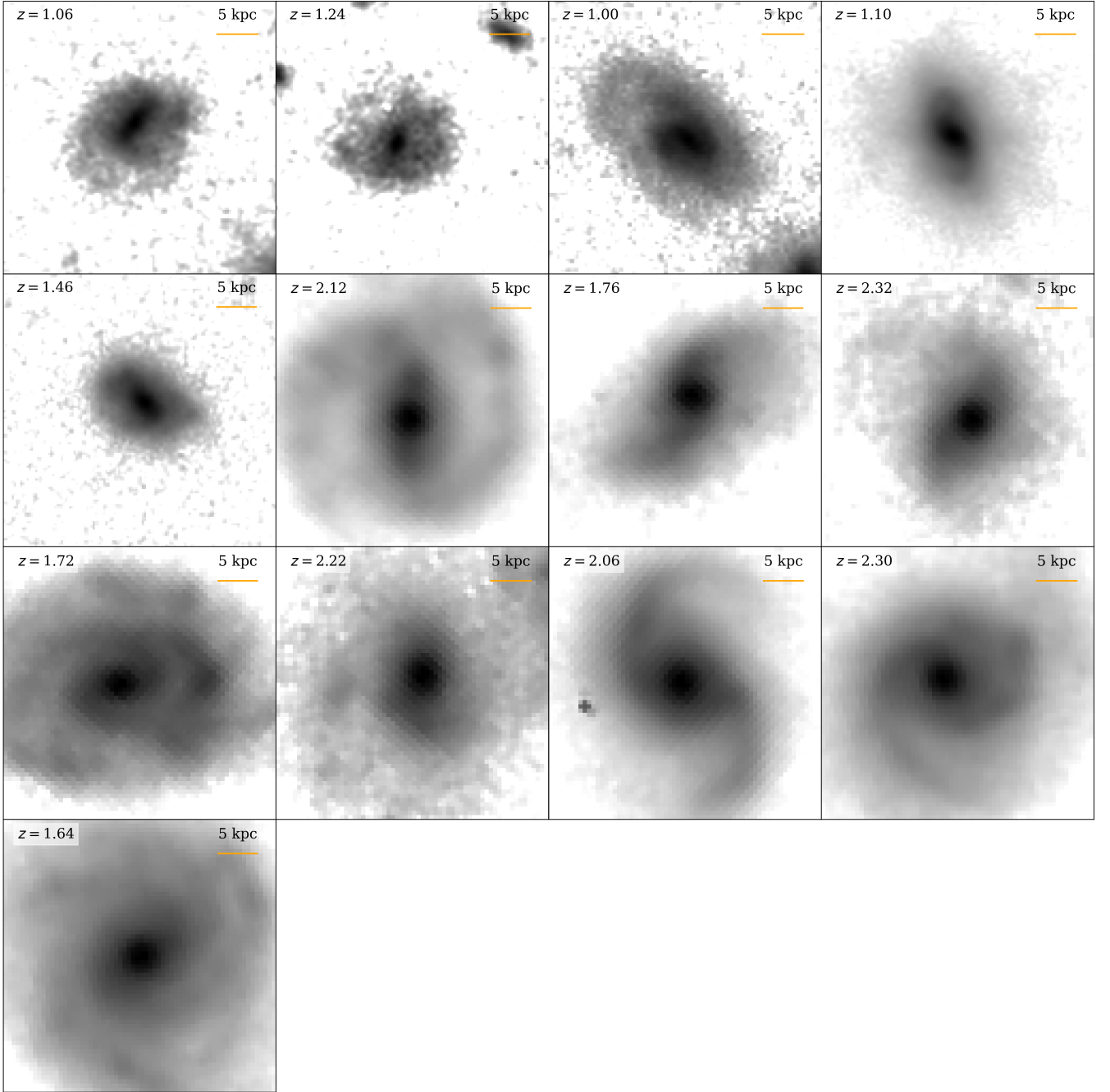


Figure A1. Rest-frame NIR logarithmic images of strongly barred galaxies using the JWST NIRCам F444W filter between the redshifts $1 \leq z \leq 3$. The redshift of the galaxy is noted in the upper left corner of each image. A 5 kpc scale is given in the upper right corner of each image (calculated using [Wright 2006](#)).

APPENDIX A: STRONGLY AND WEAKLY BARRED GALAXIES

In this study, we have visually identified CEERS galaxies as strongly barred, weakly barred or unbarred in JWST NIRCам F444W images between redshifts $1 \leq z \leq 3$. Figure A1 shows the strongly barred galaxies, while Figure A2 shows the weakly barred galaxies identified in this study.

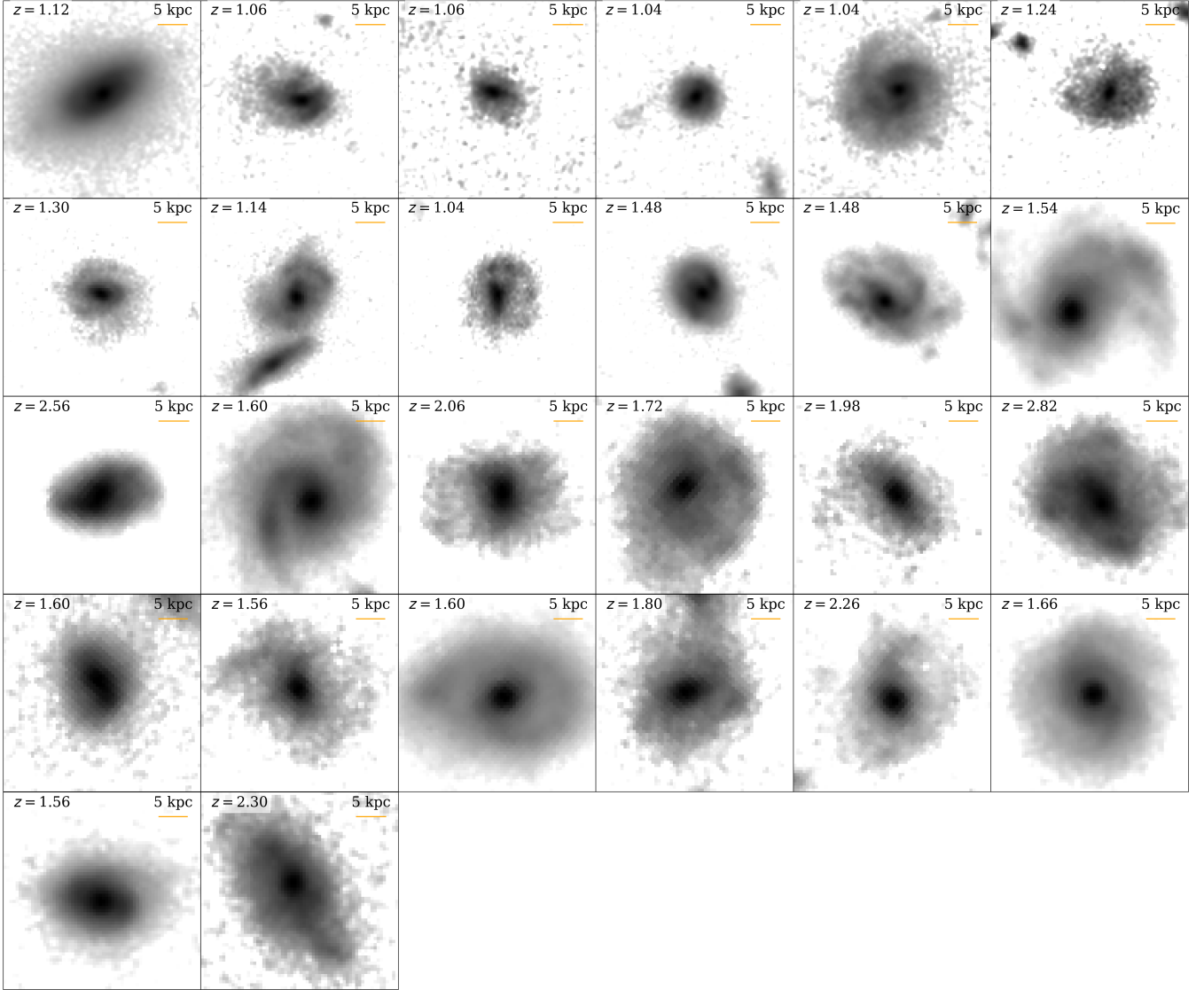


Figure A2. Rest-frame NIR logarithmic images of weakly barred galaxies using the JWST NIRCам F444W filter between the redshifts $1 \leq z \leq 3$. The redshift of the galaxy is noted in the upper left corner of each image. A 5 kpc scale is given in the upper right corner of each image (calculated using [Wright 2006](#)).

APPENDIX B: IMPACT OF INSTRUMENT SENSITIVITY ON CLASSIFICATIONS

The improved sensitivity and longer wavelength range of JWST enhance galaxy images as compared to what was previously seen in HST WFC3 images. Figure B1 shows three galaxies in the HST WFC3 F160W filter and two JWST NIRCам filters, F356W and F444W. These galaxies are interesting as they received maybe-barred or barred votes in visual classifications of HST WFC3 F160W (for a description of the method, see § 3), but unbarred votes from all classifiers in JWST NIRCам F444W. A PSF artefact (as described in § 2.1) can be identified in the JWST NIRCам images of EGS_27018 but becomes inconspicuous in the HST WFC3 image. EGS_22339 is a disc galaxy with spiral features, which could have misled visual classifications in the HST WFC3 image but is clearly unbarred in JWST NIRCам images. The only galaxy to receive barred votes in the HST WFC3 filter and unbarred votes in JWST NIRCам filters is EGS_25879, which is due to the blurring of prominent spiral arms in the F160W filter.

This paper has been typeset from a \LaTeX file prepared by the author.

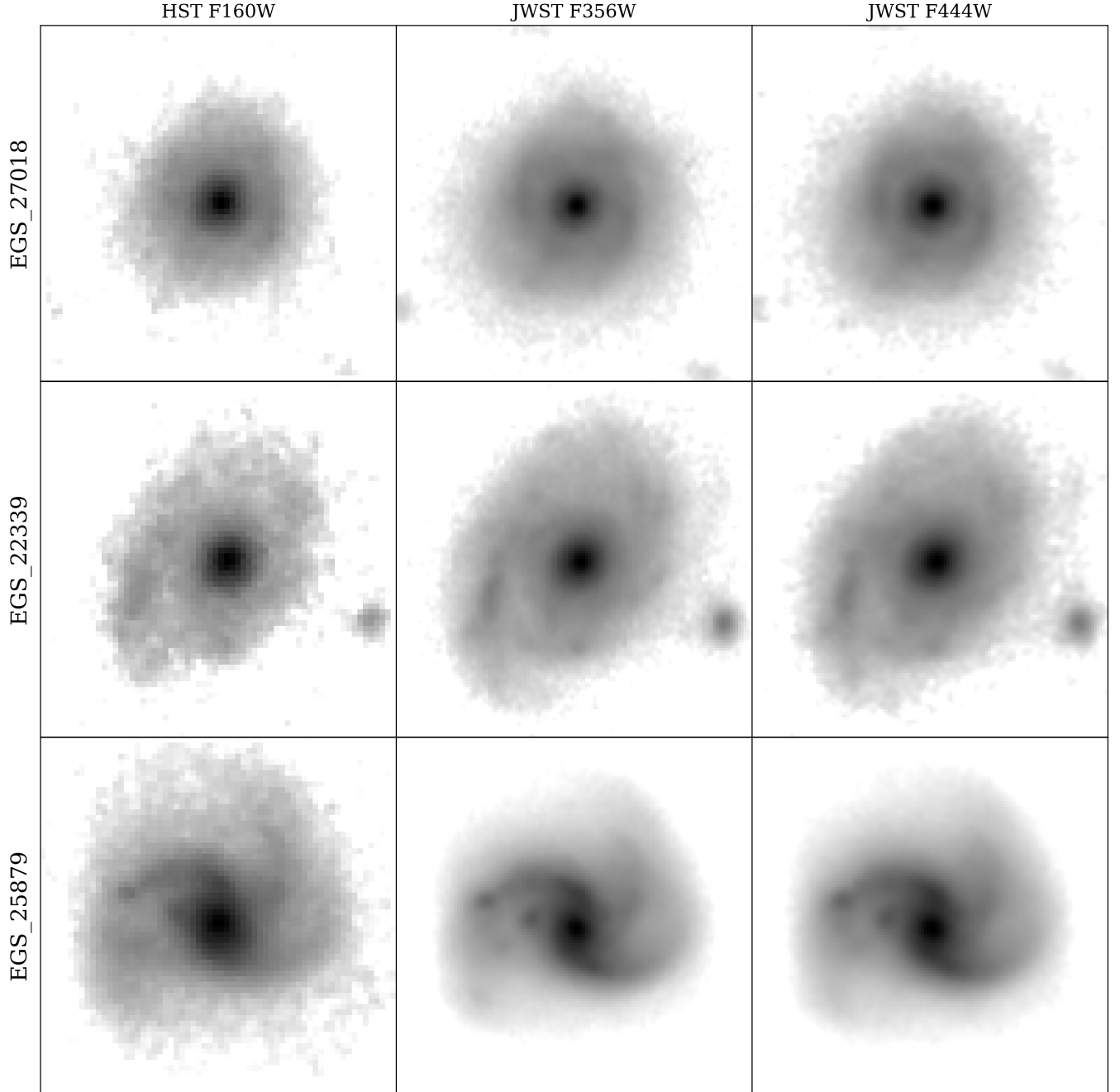


Figure B1. Logarithmic images of the galaxies EGS_27018, EGS_22339 and EGS_25879, which received maybe-barrred or barrred votes by the classifiers in the HST WFC3 F160W filter, but unbarrred votes in the JWST NIRCcam F444W filter. The three galaxies are shown in the HST WFC3 F160W (left), JWST NIRCcam F356W (middle) and JWST NIRCcam F444W (right).